Acta Crystallographica Section D
Biological Crystallography
ISSN 1399-0047

Structural basis of the transactivation deficiency of the human PPARγ F360L mutant associated with familial partial lipodystrophy

Clorinda Lori, Alessandra Pasquo, Roberta Montanari, Davide Capelli, Valerio Consalvi, Roberta Chiaraluce, Laura Cervoni, Fulvio Loiodice, Antonio Laghezza, Massimiliano Aschi, Alessandra Giorgi and Giorgio Pochetti*

Istituto di Cristallografia, CNR, Via Salaria, Km 29,300, Monterotondo Stazione, 00015 Roma, Italy

Correspondence e-mail: giorgio.pochetti@ic.cnr.it

Received 30 January 2014
Accepted 29 April 2014

PDB references: PPARγ F360L, complex with LT175, 4l96; 4l98; PPARγ R357A, complex with rosiglitazone, 4o8f

The peroxisome proliferator-activated receptors (PPARs) are transcription factors that regulate glucose and lipid metabolism. The role of PPARs in several chronic diseases such as type 2 diabetes, obesity and atherosclerosis is well known and, for this reason, they are the targets of antidiabetic and hypolipidaemic drugs. In the last decade, some rare mutations in human PPARγ that might be associated with partial lipodystrophy, dyslipidaemia, insulin resistance and colon cancer have emerged. In particular, the F360L mutant of PPARγ (PPARγ2 residue 388), which is associated with familial partial lipodystrophy, significantly decreases basal transcriptional activity and impairs stimulation by synthetic ligands. To date, the structural reason for this defective behaviour is unclear. Therefore, the crystal structure of PPARγ F360L together with the partial agonist LT175 has been solved and the mutant has been characterized by circular-dichroism spectroscopy (CD) in order to compare its thermal stability with that of the wild-type receptor. The X-ray analysis showed that the mutation induces dramatic conformational changes in the C-terminal part of the receptor ligand-binding domain (LBD) owing to the loss of van der Waals interactions made by the Phe360 residue in the wild type and an important salt bridge made by Arg357, with consequent rearrangement of loop 11/12 and the activation function helix 12 (H12). The increased mobility of H12 makes the binding of co-activators in the hydrophobic cleft less efficient, thereby markedly lowering the transactivation activity. The spectroscopic analysis in solution and molecular-dynamics (MD) simulations provided results which were in agreement and consistent with the mutant conformational changes observed by X-ray analysis. Moreover, to evaluate the importance of the salt bridge made by Arg357, the crystal structure of the PPARγ R357A mutant in complex with the agonist rosiglitazone has been solved.

1. Introduction

Peroxisome proliferator-activated receptor γ (PPARγ) is a nuclear receptor belonging to the superfamily of ligand-inducible transcription factors. Nuclear receptors are multi-domain transcription factors that bind to DNA elements and regulate gene expression. PPARs form heterodimers with the retinoid X receptor (RXR) and adopt an active conformation in the presence of a ligand. In addition, these receptors require the ligand-dependent recruitment of co-activators to create a complex that binds to peroxisome proliferator response elements (PPREs) in target genes to stimulate their expression (Nolte *et al.*, 1998; Chandra *et al.*, 2008). Three subtypes of

PPARs (α, β/δ and γ) have been identified which have distinct tissue distributions and are associated with selective ligands (Zoete *et al.*, 2007). PPARα is mainly expressed in the liver, PPARβ (also known as PPARδ) is more ubiquitously distributed and PPARγ is highly expressed in adipose tissue (Kersten *et al.*, 2000; Michalik & Wahli, 2006). PPARγ has a regulatory function in adipocyte differentiation and insulin sensitization and plays an important role in regulating lipid metabolism in mature adipocytes and macrophages (Anghel & Wahli, 2007), with a direct impact on type 2 diabetes, dyslipidaemia, atherosclerosis and cardiovascular diseases (Evans *et al.*, 2004; Semple *et al.*, 2006). In addition, PPARγ is implicated in inflammation (Mandard & Patsouris, 2013) and is expressed in many cancers, such as colon, breast and prostate cancers (Kersten *et al.*, 2000; Lehrke & Lazar, 2005; Wang *et al.*, 2006; Tontonoz & Spiegelman, 2008). PPARγ is the target of antidiabetic thiazolidinedione (TZDs) drugs including troglitazone, rosiglitazone, pioglitazone and ciglitazone (Schoonjans & Auwerx, 2000). There is evidence that some rare missense mutations in PPARγ have profound phenotypic effects in affected individuals, contributing to the risk of insulin resistance, dyslipidaemia, type 2 diabetes (Chan *et al.*, 2013) and colon cancer (Semple *et al.*, 2006; Barroso *et al.*, 1999; Sarraf *et al.*, 1999; Savage *et al.*, 2003; Meirhaeghe & Amouyel, 2004; Agostini *et al.*, 2006; Tan *et al.*, 2008; Jeninga *et al.*, 2009). Some of these mutations can be associated with partial lipodystrophy (Al-Shali *et al.*, 2004; Li & Leff, 2007). Lipodystrophy is a group of conditions characterized by a generalized or partial loss of adipose tissue associated with severe insulin resistance, hypertriglyceridaemia and diabetes (Monajemi *et al.*, 2007; Guettier *et al.*, 2008). In this study, we investigated the effects of the F360L mutation on the structure and thermal stability of human PPARγ. This mutation is located in the LBD of the receptor and is associated with autosomal dominant familial partial lipodystrophy (FPLD; Hegele *et al.*, 2002; Hegele, 2005). This metabolic disease is characterized by adipose-tissue repartitioning with multiple metabolic disturbances, including insulin resistance and dyslipidaemia. To date, the structurally disruptive effect of this missense mutation is unknown. In order to gain more insight into the effects of such a mutation at a molecular level, we unsuccessfully tried to crystallize the apo form of the mutant in the same conditions used to crystallize the apo form of wild-type (WT) PPARγ (Nolte *et al.*, 1998). With the aim of making the LBD of PPARγ more stable, in this way favouring its crystallization, we decided to perform co-crystallization trials with a ligand. The crystal structure of the complex between the F360L mutant of PPARγ and the ligand LT175, an analogue of clofibric acid with a partial agonism profile towards PPARγ, has been determined. This ligand was selected because LT175 occupies the diphenyl pocket (Montanari *et al.*, 2008), a region of the LBD which is also formed by the loop containing the mutated Phe360 residue. A comparison of this structure with the previously solved complex structure (Montanari *et al.*, 2008) of the WT receptor with the same ligand (PDB entry 3b3k) would have allowed us to verify the consequences of the mutation for ligand binding. Crystallization trials were also performed with the full agonist rosiglitazone, but they did not produce crystals suitable for X-ray analysis. Given the failure to crystallize the apo form of the mutant, MD simulations were also performed on the F360L mutant to evaluate the effects of this mutation in the absence of ligands. Moreover, the PPARγ mutant R357A was also expressed and its complex with rosiglitazone was analyzed by X-ray crystallography to study the important role played by the Arg357 residue in stabilizing the diphenyl pocket. Co-crystallization of the R357A mutant with the ligand LT175 was not successful. The effects of these mutations were also studied by evaluating the transcription activity of the full agonist rosiglitazone and LT175 towards PPARγ, PPARγ F360L and PPARγ R357A in a PPARγ–Gal4 transactivation assay. Finally, spectroscopic characterization and microcalorimetric experiments were performed in order to compare the F360L mutant with the WT receptor and to evaluate the affinity of the coactivator SRC-1 for the WT and the mutants.

2. Materials and methods

2.1. Plasmids and site-directed mutagenesis

The PPARγ LBD wild type (gene ID 5468, amino acids 174–477, expected molecular mass 34.5 kDa) and the F360L and R357A mutants were cloned in pET-28 plasmid for *Escherichia coli* expression as previously described (Pochetti *et al.*, 2007). The QuikChange Site-Directed Mutagenesis Kit (Stratagene) was used to introduce the point mutations into the bacterial expression vector and into the vector expressing the chimeric receptor containing the yeast Gal4 DNA-binding domain fused to the wild-type PPARγ LBD used for the transcription-activity assay (Raspé *et al.*, 1999). The mutagenic synthetic oligonucleotides are shown in Supplementary Table S1[1].

2.2. Cell culture and transfections

The human hepatoblastoma cell line HepG2 (Interlab Cell Line Collection, Genoa, Italy) was cultured in minimum essential medium (MEM) containing 10% heat-inactivated foetal bovine serum, 100 U ml^{-1} penicillin G and 100 µg ml^{-1} streptomycin sulfate at 310 K in a humidified atmosphere of 5% CO_2. For transactivation assays, 10^5 cells per well were seeded in a 24-well plate and transfections were performed after 24 h with CAPHOS, a calcium phosphate method, according to the manufacturer's guidelines. Cells were transfected with expression plasmids encoding the fusion protein Gal4–PPARγ LBD (30 ng), pGal5TKpGL3 (100 ng) and pCMV-β-gal (250 ng). 4 h after transfection, the cells were treated for 20 h with the indicated ligands in triplicate. The luciferase activity in the cell extracts was then determined using a luminometer (VICTOR^3 V Multilabel Plate Reader, PerkinElmer). The β-galactosidase activity was determined using *ortho*-nitrophenyl-β-D-galactopyranoside as described

[1] Supporting information has been deposited in the IUCr electronic archive (Reference: BE5257).

Table 1
Data-collection and refinement statistics.

Values in parentheses are for the outermost resolution shell.

	PPARγ F360L (sodium formate)	PPARγ F360L (sodium/potassium phosphate)	PPARγ R357A
Data collection			
Space group	$P2_12_12$	$I222$	$C222_1$
Unit-cell parameters			
a (Å)	64.41	67.17	85.70
b (Å)	112.46	112.00	87.10
c (Å)	117.74	116.80	163.8
X-ray source	ESRF	ESRF	ESRF
No. of molecules in asymmetric unit	2	1	2
Wavelength (Å)	0.973	0.973	0.976
Resolution (Å)	50–2.28 (2.50–2.28)	41–2.38 (2.47–2.38)	82–2.56 (2.72–2.60)
Unique reflections	39713	17959	18994
Completeness (%)	99.9 (99.9)	100 (99.3)	98.8 (97.5)
R_{merge} (%)	8.8 (42.4)	11.0 (60.1)	6.1 (43.5)
$\langle I/\sigma(I)\rangle$	18.9 (4.8)	11.3 (2.9)	9.3 (1.3)
Refinement			
R_{cryst} (%)	21.4	18.9	23.8
R_{free} (%)	25.6	22.7	29.6
R.m.s.d., bonds (Å)	0.012	0.011	0.015
R.m.s.d., angles (°)	1.45	1.43	1.58
No. of residues used in refinement†			
Molecule *A*	244	260	252
Molecule *B*	258	—	249
Ligands	2	1	2
Waters	227	126	61
Wilson B (Å^2)	36.6	27.0	57.6
Mean B factors (Å^2)			
Protein	44.1	46.0	80.7
Ligands	24.2	28.3	85.9
Waters	36.9	44.2	73.6
Ramachandran plot‡			
Outliers (%)	1.2	1.2	2.3
Favoured (%)	97.0	94.5	89.9
Rotamer outliers (%)	2.0	2.6	3.1
PDB code	4l98	4l96	4o8f

† The omitted atoms belong to disordered loops with poor electron density. ‡ These parameters were taken from the the *MolProbity* model-validation suite in *PHENIX* (Chen *et al.*, 2010).

previously (Hollon & Yoshimura, 1989). All transfection experiments were repeated at least twice.

2.3. Protein preparation and crystallization

PPARγ wild type, F360L and R357A were expressed as N-terminally His-tagged proteins using pET-28 vector and were then purified as follows. Freshly transformed *E. coli* BL21 (DE3) cells were grown in LB medium with 30 µg ml^{-1} kanamycin at 310 K to an OD of 0.6. The culture was then induced with 0.1 m*M* isopropyl β-D-thiogalactopyranoside and further incubated at 291 K for 20 h with vigorous shaking. Cells were harvested and resuspended as a 20 ml l^{-1} culture in buffer *A* [20 m*M* Tris, 150 m*M* NaCl, 10% glycerol, 1 m*M* tris(2-carboxyethyl)phosphine–HCl (TCEP) pH 8.0] in the presence of protease inhibitors (Complete Mini EDTA-free; Roche Applied Science). The cells were sonicated and the soluble fraction was isolated by centrifugation (35 000*g* for 45 min). The supernatant was loaded onto an Ni^{2+}–nitrilotriacetic acid column (GE Healthcare) and eluted with a gradient of 0–300 m*M* in buffer *A* (batch method). The pure fractions were concentrated to 2 ml using Millipore concentrators and loaded onto a Superdex 200 300/10 gel-filtration column on an ÄKTA FPLC system previously equilibrated with 50 m*M* Tris–HCl, 0.25 *M* NaCl, 2 m*M* DTT pH 8.0 at a flow rate of 1.0 ml min^{-1}. The collected eluates were tested for purity by SDS–PAGE. The pure proteins were identified by MALDI-TOF AutoFlex II mass-spectrometric analysis (Bruker Daltonics, Bremen, Germany). SDS–PAGE bands were cut from the gel and processed *via* tryptic proteolysis. The peptide mixtures were manually analyzed by the *FlexAnalysis* program (Bruker Daltonics, Bremen, Germany) and revealed the expected site mutations. The protein was then cleaved with thrombin protease (GE Healthcare; 10 U mg^{-1}) at room temperature for 2 h. The digested mixture was reloaded onto an Ni^{2+}–nitrilotriacetic acid column to remove the His tag and the undigested protein. The flowthrough was loaded onto a Q-Sepharose HP column (GE Healthcare) and eluted with a 0–500 m*M* gradient of NaCl in buffer *B* (20 m*M* Tris, 10% glycerol, 1 m*M* TCEP pH 8.0) with a BioLogic DuoFlow FPLC system (Bio-Rad Laboratories, Italy). Finally, the protein was purified by gel-filtration chromatography on a HiLoad Superdex 75 column (GE Healthcare) and eluted with buffer *C* (20 m*M* Tris, 1 m*M* TCEP, 0.5 m*M* EDTA pH 8.0). The protein was then concentrated to 8–10 mg ml^{-1} using Amicon centrifugal concentrators with a 10 kDa cutoff membrane (Millipore, USA). The protein complexes with the ligands were formed by mixing 98 µl protein solution with 2 µl ligand stock solution (50 m*M* in DMSO) so that the ligands were in a threefold excess with respect to the protein. The mutant complexes in buffer *C* were used for crystallization at 293 K by the vapour-diffusion method in 96-well sitting-drop plates (MRC plates; Molecular Dimensions, UK). Preliminary crystallization trials of the mutant complexes were performed with a Phoenix liquid-handling robot (Art Robbins) by mixing 200 nl protein solution with an equal volume of reservoir solution (Biocrystal Facility at the CNR Institute of Biology and Molecular Pathology, Sapienza University of Rome). Crystals of PPARγ F360L with LT175 (referred to in the following as F360L) appeared in well Nos. 18 (0.35 *M* sodium dihydrogen phosphate, 0.65 *M* dipotassium hydrogen phosphate pH 6.9) and 25 (3.5 *M* sodium formate pH 7.0) of the Index crystallization kit (Hampton Research). More suitable crystals for X-ray analysis were then obtained by the vapour-diffusion method at 291 K using a sitting drop made by mixing 2 µl protein–ligand

solution (8 mg ml^{-1} in 20 m*M* Tris, 1 m*M* TCEP pH 8.0) with 2 µl reservoir solution (3.3 *M* sodium formate pH 7.0 or 1 *M* sodium/potassium phosphate pH 6.9) and equilibrating against 0.5 ml reservoir buffer. Crystals appeared after a few days from both tested conditions and belonged to space group $P2_12_12$ or $I222$, respectively. Crystals were flash-cooled in liquid nitrogen after brief soaking in a cryoprotectant buffer [mother-liquor solution with 20%(*v*/*v*) glycerol]. Crystals of R357A with rosiglitazone (referred to in the following as R357A) appeared in well No. 5 (30% PEG 550 MME/PEG 20K, 0.06 *M* $MgCl_2$ and $CaCl_2$, 0.1 *M* sodium HEPES and MOPS pH 7.5) of the Morpheus crystallization kit (Molecular Dimensions, UK). Suitable crystals were directly flash-cooled in liquid nitrogen.

2.4. Data collection, structure determination and refinement

X-ray data were collected at 100 K under a nitrogen stream using synchrotron radiation (beamlines ID23-2 for F360L and ID29 for R357A at ESRF, Grenoble, France). The collected data were processed using *MOSFLM* (Battye *et al.*, 2011) and *SCALA* for the crystal of F360L belonging to space group $I222$ and *XDS* and *XSCALE* (Kabsch, 2010) for that belonging to space group $P2_12_12$. Structure solution was performed with *AMoRe* (Navaza, 1994) using the coordinates of PPARγ–LT175 (PDB entry 3b3k; Montanari *et al.*, 2008) as the starting model. The coordinates were then refined with *CNS* (Brünger *et al.*, 1998). Finally, both refined models were optimized by the *PDB_REDO* web server using *REFMAC*5.8.0049 (Murshudov *et al.*, 2011). *MOSFLM* and *SCALA* were used to process the R357A data. Structure solution was performed with *AMoRe* using the coordinates of PPARγ–rosiglitazone (Nolte *et al.*, 1998; PDB entry 2prg). The coordinates were then refined with *PHENIX* (Adams *et al.*, 2010). The quality of the structures was validated using *MolProbity* (Chen *et al.*, 2010). The statistics of the crystallographic data and refinement are summarized in Table 1.

2.5. Isothermal titration calorimetry (ITC)

ITC experiments were performed at 25°C using a MicroCal ITC_{200} microcalorimeter (MicroCal Inc., Northampton, Massachusetts, USA). PPARγ was extensively dialyzed against 20 m*M* HEPES pH 8.0, 1 m*M* TCEP with Amicon Ultra filters and the final exchange buffer was then used to dilute the ligand stock solution (50 m*M* in DMSO). DMSO was added to the protein solution at the same percentage as the ligand solution (1%). In all of the experiments the protein solution (25–50 µ*M*) was placed in the sample cell and the co-activator SRC-1 (500 µ*M*) was loaded into the syringe injector. The experiments with SRC-1 (purchased from GL Biochem Ltd, Shanghai, People's Republic of China) were performed after equilibrating the protein with LT175 in a 2:1 excess. The titrations involved 19 injections of 2 µl at 180 s intervals. The syringe stirring speed was set at 1000 rev min^{-1}. Reference titrations of co-activator into the buffer were used to correct for heats of dilution. The thermodynamic data were processed with the *Origin* 7.0 software provided by MicroCal. The ΔH values were measured for each titration and fitting the binding isotherms with a one-site binding model gave the values of the association constants (K_a). The inflection point in the calorimetric isotherm gives the stoichiometry value *n*, indicating the ligand:protein ratio of the binding.

2.6. Spectroscopic measurements and thermal denaturation experiments

Intrinsic fluorescence emission measurements were carried out at 283 K in 20 m*M* Tris–HCl pH 8.0 containing 0.1 *M* NaCl with an LS50B spectrofluorimeter (PerkinElmer) at 90.0 µg ml^{-1} protein concentration (0.2 m*M* DTT) using a 1.0 cm path-length quartz cuvette. Fluorescence emission spectra were recorded from 290 to 450 nm (1 nm sampling interval) with the excitation wavelength set to 274 nm. Far-UV (190–250 nm) and near-UV (250–310 nm) CD spectra were recorded at a protein concentration of 4.60 mg ml^{-1} (2.0 m*M* DTT) and were measured using 0.01 and 1.0 cm path-length quartz cuvettes, respectively. The results obtained were expressed as the mean residue ellipticity [Θ], assuming a mean residue molecular mass of 110 per amino-acid residue. Far-UV and near-UV CD spectra were obtained at 293 K in 50 m*M* Tris–HCl pH 8.0 containing 0.25 *M* NaCl. In the thermal denaturation experiments, PPARγ WT and F360L (0.20 mg ml^{-1} in 20 m*M* Tris–HCl pH 8.0, 0.20 *M* NaCl, 0.2 m*M* DTT) were heated from 293 to 343 K in a 0.1 cm path-length quartz cuvette with a heating rate of 1 K min^{-1} controlled by a Jasco programmable Peltier element. The dichroic activity at 222 nm and the PMTV were continuously monitored in parallel every 0.5 K. All of the thermal scans were corrected for the solvent contribution at the different temperatures. Melting-temperature (T_m) values were calculated by taking the first derivative of the ellipticity at 222 nm with respect to temperature. All denaturation experiments were performed in triplicate.

2.7. Molecular-dynamics simulations

The molecular-dynamics (MD) simulations were performed utilizing the *Gromacs* package (Van Der Spoel *et al.*, 2005). The initial coordinates of the WT receptor were taken from the crystal structure of the PPARγ–rosiglitazone complex (Nolte *et al.*, 1998). The coordinates of the mutant were adapted from the WT coordinates by performing a point mutation. Each system was placed in a dodecahedral box, the dimensions of which prevent self-interaction, which was filled with 14 770 water molecules at the typical density of water at 298 K and 1.0 atm, utilizing the single point charge (SPC) model (Berendsen *et al.*, 1981). Both simulations were performed adopting the protocol described below. After an energy minimization, the whole system was slowly heated to 300 K using short (100.0 ps) MD runs. The resulting configurations were used to start the simulations, which were propagated up to 68.0 ns. The isothermal/isochoric ensemble was adopted in all of the simulations, making use of the Berendsen thermostat (Berendsen *et al.*, 1984). The OPLS force field (Jorgensen *et al.*, 1996) and the *LINCS* algorithm

(Hess *et al.*, 1997) were used in conjunction with the Particle Mesh Ewald method (Darden *et al.*, 1993) with 34 wavevectors in each dimension and a fourth-order cubic interpolation for the long-range electrostatics. Much of the collective analysis used in this work is based on essential dynamics (ED; Amadei *et al.*, 1993). On purpose, the covariance matrix of the atomic positional fluctuations (either all atoms or backbone; see §3) was built from the MD trajectory and then diagonalized, producing an orthonormal set of eigenvectors defining a new set of generalized coordinates along which the protein fluctuations occur. The trace of the covariance matrix provides us with a direct measure of the extent of the overall fluctuations of the WT and mutant receptor.

3. Results

3.1. Overall structure of PPARγ F360L

Crystals of PPARγ F360L–LT175 were obtained from two different conditions (sodium/potassium phosphate and sodium formate) and they belonged to different space groups (*I*222 and $P2_12_12$), with one and two molecules in the asymmetric unit, respectively (Table 1). Accurate observation of both of the structures revealed that the crystal packing is almost the same with an identical arrangement of the single monomers (r.m.s.d. of 0.53 and 0.63 Å, respectively, for the two monomers in $P2_12_12$ superimposed onto the monomer of *I*222) and of the homodimer. Comparing the PPARγ F360L–LT175 crystal structure (space group $P2_12_12$) with that of the WT receptor also complexed with LT175, it can be noticed that the interface between the two monomers of the homodimer in PPARγ F360L–LT175 is different from that of PPARγ WT–LT175 and of all the known crystal structures of the WT complexed with other ligands. The WT interface is formed by helices 11 and 10 of the two monomers, which face each other (Fig. 1*a*), while the PPARγ F360L interface is formed by helices 3, 12 and loop 11/12 of each molecule (Fig. 1*b*). An analysis of the dimerization interface of F360L with the

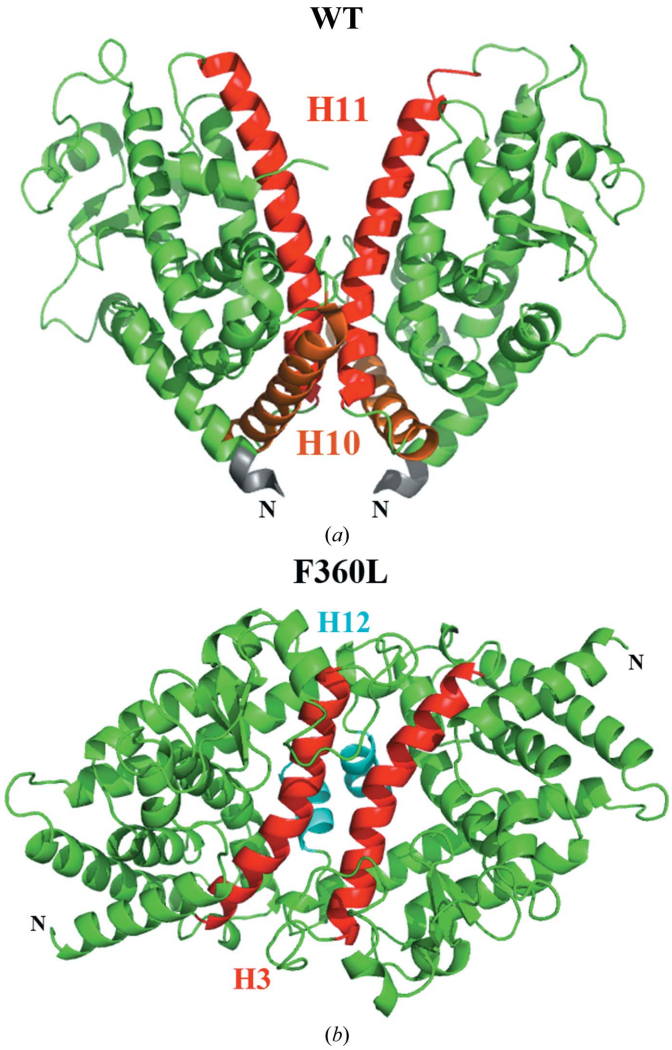

Figure 1
Homodimer of the WT (*a*) and the F360L mutant (*b*). The interface between the monomers is drawn in red, orange and cyan.

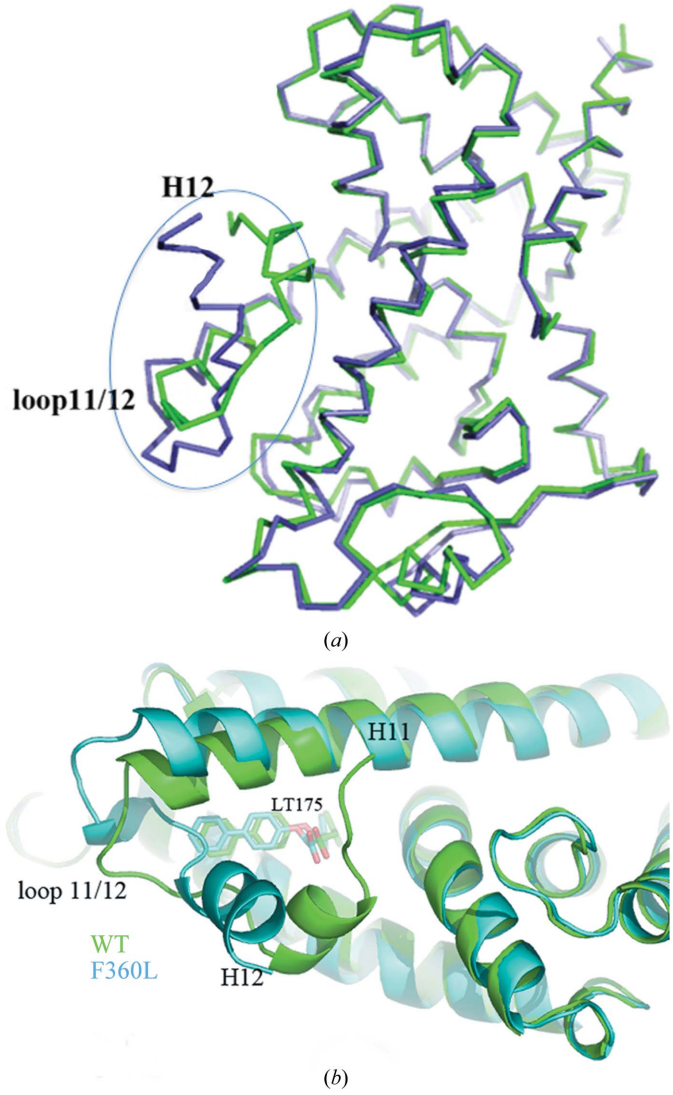

Figure 2
(*a*) Superposition of the crystal structures of the WT (green) and the F360L mutant (cyan) complexed with the ligand LT175. The regions with the main conformational differences are included in the ellipse. (*b*) An enlargement of helices H11, H12 and loop 11/12 is shown.

program *PSAP* (*Protein Structure Analysis Package*; Balamurugam *et al.*, 2007) revealed that this new arrangement of the dimer in PPARγ F360L is very stable, with five salt bridges and 21 hydrogen bonds and a more extended surface of interaction between the two monomers with respect to the WT.

3.2. Conformational changes in the monomer induced by the F360L mutation

The superposition of a single monomer of WT and F360L PPARγ shows that the two molecules have similar conformations, with the exception of the terminal end of helix 11, loop 11/12 and helix 12 (Figs. 2*a* and 2*b*). A more careful observation of the structures shows that the strong van der Waals interactions made by the side chain of Phe360 in the WT with the side chains of Ile279 in helix 3 and Ile456 in helix 11 (3.2 and 3.7 Å, respectively) are lost in the mutant (6.2 and 5.4 Å, respectively), denoting a key role of Phe360 in stabilizing this region of the LBD (the diphenyl pocket; Fig. 3*a*). Destabilization of the terminal end of helix 11 owing to the F360L mutation and the consequent rearrangement of the following loop 11/12 allows a different stabilization of this region, whereas a pivotal role is played by the side chain of Leu465 in loop 11/12, which forms van der Waals contacts with Leu360 and Ile279 (3.8 and 3.2 Å, respectively; Fig. 3*b*).

Moreover, the very strong salt bridge present in the WT between Arg357, belonging to loop 6/7, and Glu460, in loop 11/12, is partially lost in the mutant (the shortest distance increases from 2.6 to 5.2 Å, respectively; Fig. 3*c*). Another salt bridge between Arg357 and Glu276 in helix 3 is also weakened (the shortest distance increases from 2.8 to 4.1 Å, respectively). This could be also owing to the loss of interaction between the positively charged Arg357 and the polarizable π-electron cloud of the aromatic ring of Phe360 (the shortest distance between the two residues is 3.4 Å). This is a common interaction in proteins that provides conformational tethering of the arginine side chain while leaving its hydrogen-bond capacity intact for use in the binding of acidic residues (Flocco & Mowbray, 1994). The shorter leucine is not able, using only van der Waals interactions, to stabilize the side chain of Arg357, which loses the salt bridge with Glu460, in this way destabilizing loop 11/12 in which Glu460 is located.

As mentioned above, the changed van der Waals interaction network in the region of the diphenyl pocket and the weakening of the salt bridges Arg357–Glu460 and Arg35–Glu276 provoke a dramatic rearrangement of the mutant loop 11/12, which assumes a different conformation with respect to the WT (Fig. 4*a*), with the side chain of His466 playing a critical role in the different stabilization of this loop and of helix 12

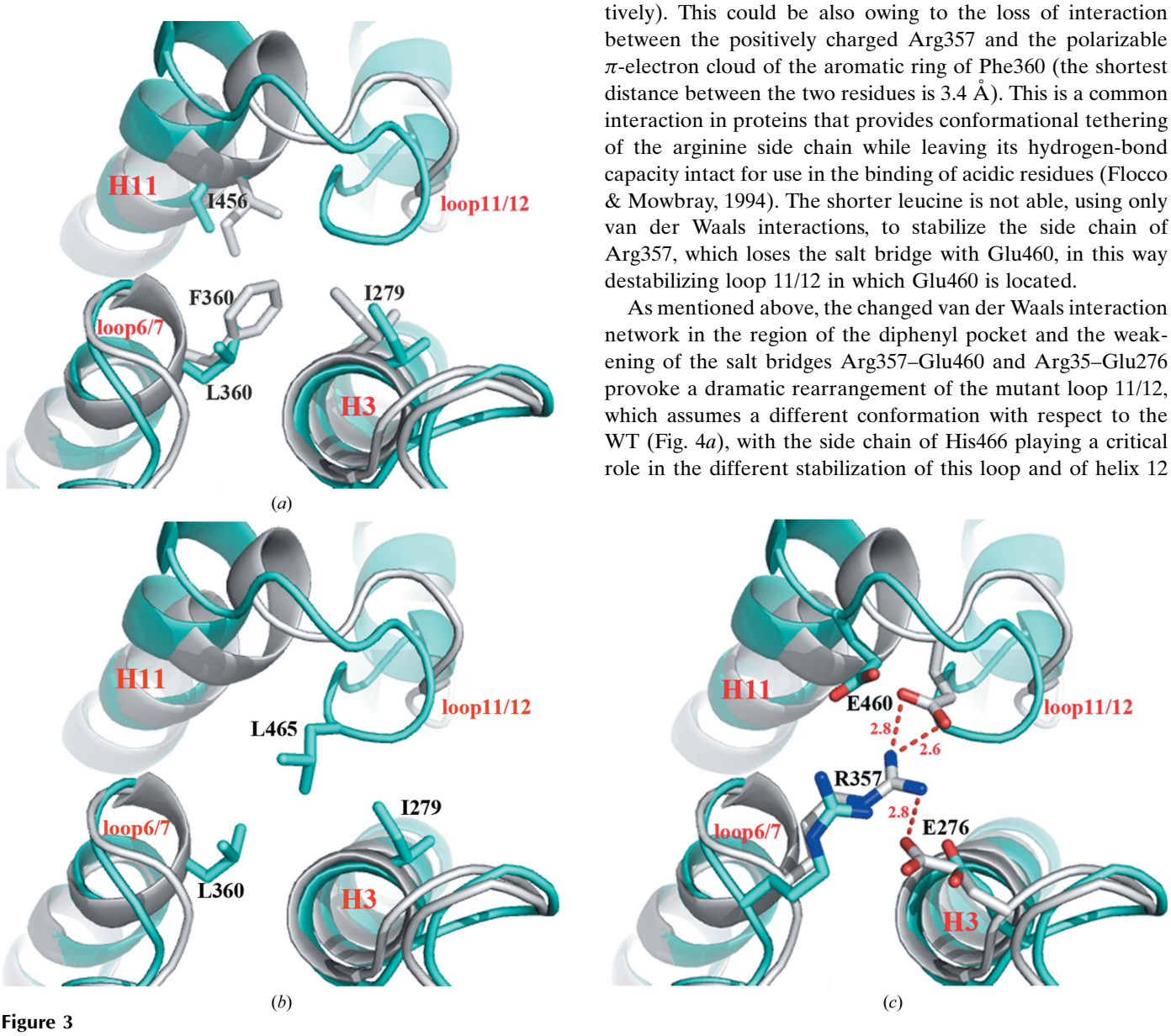

Figure 3
Superposition of the crystal structures of the WT (white) and the F360L mutant (cyan) complexed with the ligand LT175. (*a*) Van der Waals interactions between residues of H3, H11 and loop 6/7; (*b*) van der Waals interactions of loop 6/7 with loop 11/12 and helix 3 in the F360L mutant; (*c*) electrostatic interactions of Arg357 with Glu460 and Glu276. Hydrogen bonds are depicted as red dashed lines.

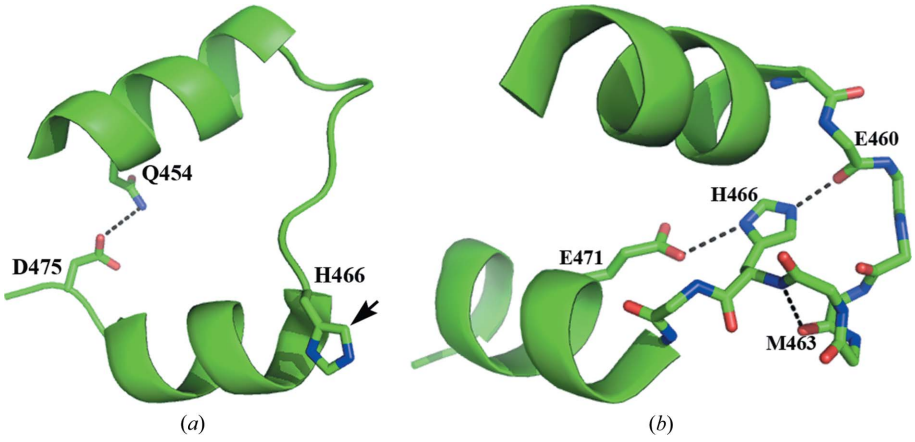

Figure 4
Conformation of loop 11/12 in (*a*) the WT and (*b*) the F360L mutant. Hydrogen bonds are drawn as black dashed lines; the black arrow indicates the different position of the His466 side chain in the WT.

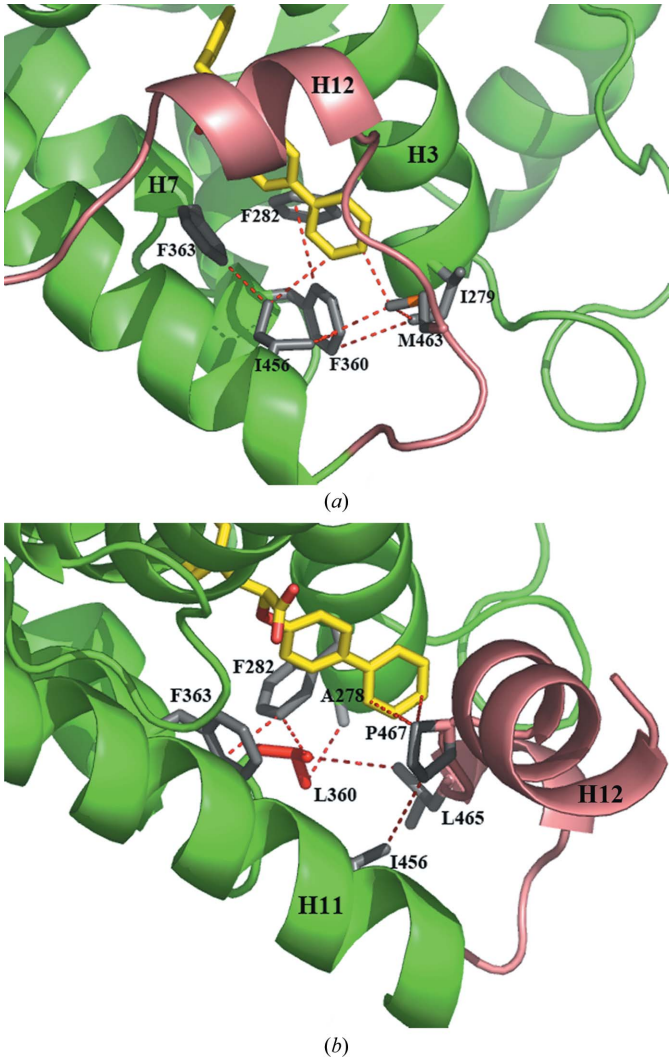

Figure 5
Van der Waals interactions in the diphenyl pocket of (*a*) the WT and (*b*) the F360L mutant. The mutated residue Leu360 is depicted in red and the ligand LT175 in yellow.

(H12) (Fig. 4*b*). Moreover, in the mutant structure the new conformation of loop 11/12 is stabilized by a direct van der Waals interaction (3.8 Å) between the side chains of Leu465 and the mutated Leu360 (Fig. 3*b*). In Fig. 5 the different networks of van der Waals interactions at the bottom of diphenyl pocket in the mutant and WT are shown. It is possible to observe that Leu360 of the mutant makes van der Waals contacts with Phe282 and Ala278 in H3 (3.1 and 3.4 Å, respectively) and Leu465 in loop 11/12 (3.8 Å), while in the WT the shortest van der Waals contacts of Phe360 are with the side chain of Phe282 and Ile279 belonging to H3 (3.5 and 3.3 Å, respectively) and Ile456 in H11 (3.6 Å). Phe360 and Phe282 are also involved in a typical 'edge-to-ring face' interaction between the Phe aromatic rings. It is worth noting that the important role played by Met463 of WT in the interaction with the terminal end of the LT175 ligand (Fig. 5*a*) is assumed by Pro467 (Fig. 5*b*) in the mutant. The final result of all of these conformational changes induced by the mutation F360L is that the transactivation helix 12 assumes a different and inactive conformation (Figs. 2 and 5*b*).

3.3. Ligand interactions

Figs. 2(*b*) and 5(*b*) show that LT175 maintains the same position in the F360L LBD (the OMIT maps calculated around the ligand are shown in Supplementary Figs. S1*a*–*c*), although inserted more deeply in the pocket, with similar van der Waals contacts; the only exception is the already discussed interaction with Pro467 at the bottom of the diphenyl pocket. On the contrary, the main difference is the hydrogen-bond network made by its carboxylate O atoms. Besides the canonical interaction with histidines His449 and His323, the two O atoms make hydrogen bonds to Tyr473 and Tyr477 in helix 12, both belonging to the facing molecule of the homodimer (Fig. 6*a*). Therefore, there is an additional tyrosine, Tyr477, that is engaged in hydrogen bonds to the carboxylate group besides the canonical Tyr473, which, however, in the WT homodimer belongs to the same monomer where the ligand is bound. This very stable arrangement, as denoted by well defined electron densities of all the residues of H12, is made possible by the new interface between the two monomers, in which H12 of one molecule protrudes towards the ligand inserted into the LBD of the facing molecule (Fig. 6*b*). This is probably an artifact of the crystal packing: the destabilization of H12 caused by the mutation allows this helix to find a new conformation that favours a new stable interface between two monomers in the crystal.

It is worth noting that despite several trials it was not possible to crystallize the apo form of the mutant in the conditions generally used to crystallize the WT apo form,

Table 2
Results of MD simulations for PPARγ WT and the F360L mutant.

The standard deviations are reported in parentheses.

	WT	F360L
Backbone r.m.s.d. (nm)	2.59×10^{-1} (1.57×10^{-2})	2.75×10^{-1} (2.44×10^{-2})
Radius of gyration (nm)	1.95 (1.0×10^{-2})	1.95 (1.1×10^{-2})
Trace of the covariance matrix (nm^2)	10.9 (0.5)	13.2 (0.6)

suggesting that the mutation destabilizes the LBD of PPARγ and the active conformation of H12 and only the presence of the ligand allows the complex to crystallize, albeit through a new dimer interface.

3.4. MD simulations

In order to check the results of the X-ray analysis, MD simulations were also performed on the apo form of F360L and the WT. Table 2 contains the basic data concerning the simulated systems. The backbone root-mean-square deviation (r.m.s.d.) evaluated for both the WT and F360L with respect to the initial structure of the WT (PDB entry 1prg; Nolte *et al.*, 1998), characterized by a relatively low value, indicates that the average structure of both of the macromolecules in solution is not dramatically different from that found in the crystalline state. Also, the close values of the radius of gyration reported in Table 2 suggest a strong average morphological similarity of the WT and the F360L mutant. On the other hand, the high difference in the trace of the backbone covariance matrix, which concisely provides us with the whole internal fluctuation of the macromolecules, clearly shows that the point mutation produces a sharp mechanical destabilization of the whole system accompanied by a very large increase in the whole fluctuation. This is further confirmed by analysis of the root-mean-square fluctuation (r.m.s.f.) per residue, as reported in Fig. 7(*a*), where it is possible to appreciate the increase of the fluctuation of the F360L mutant in the marked regions which specifically correspond to H12 and residues 280–287 of H3. The H12 destabilization induced by the F360L mutation is also revealed through analysis of the interfragment distances, as reported in Fig. 7(*b*). In fact, a sharp strengthening and lengthening of the mutual interaction between H12 and the subportion 280–287 of H3 in the WT and the F360L mutant, respectively, can be observed. Moreover, in the simulation, residue 360, in both the WT and the mutant, is found to be surrounded at relatively close distances (less than 4 Å) by the following four residues: Ala278, Ile279, Phe282 and Ile456. Fig. 7(*c*) reports the mobility (r.m.s.f.) of these residues. The result indicates that the change from Phe to Leu at position 360 produces a sharp increase in the r.m.s.f., *i.e.* a weakening of the nonbonding interaction, for residues Ile279 and Ile456.

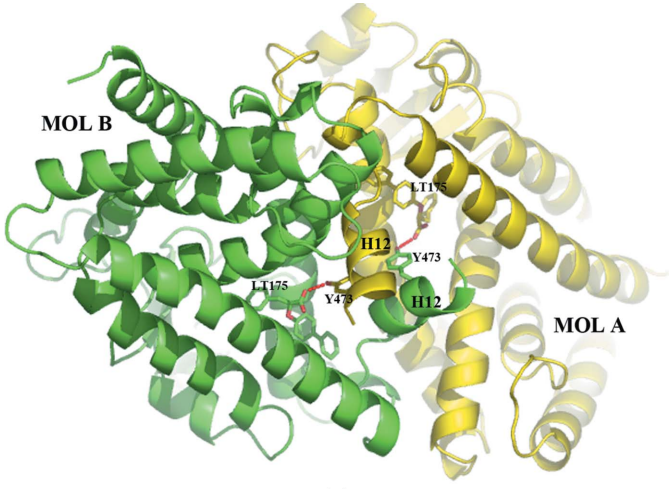

(*a*)

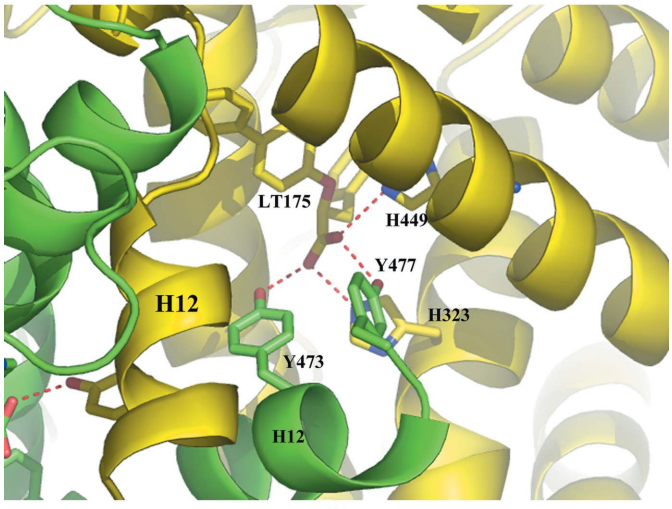

(*b*)

Figure 6
(*a*) PPARγ homodimer of the F360L mutant (monomer *A* in yellow and monomer *B* in green); (*b*) hydrogen bonds made by residues of monomer *A* (yellow) and monomer *B* (green) of the homodimer with the carboxylate group of the ligand LT175 (yellow).

3.5. Crystal structure of the complex between R357A and rosiglitazone

In order to check the importance of the residue Arg357 in the stabilization of the LBD, we solved the structure of the PPARγ R357A mutant complexed with the potent agonist rosiglitazone. The PPARγ R357A–rosiglitazone complex crystallized in space group $C222_1$ with two molecules in the asymmetric unit (Table 1). A comparison with the crystal structure of the WT with the same ligand (PDB entry 2prg; Nolte *et al.*, 1998) showed that the complex of the mutant maintains the same dimer interface and the same monomer conformation with H12 in the active form. However, an accurate examination of the *B* factors of the mutant reveals a general increase in the thermal parameters with respect to the WT, particularly for the atoms in loop 6/7 containing the mutation, in the region 276–282 in helix 3 and in the region 453–475 including the terminal part of H11 and loop 11/12 (Supplementary Fig. S2), as found in the MD simulation of apo F360L and in the crystal structure of F360L–LT175. In particular, the electron density around the side chains of Ile279 and Ile456, contacting Phe360, is very weak. Super-

position of the crystal structures of R357A and the WT shows that the ligands occupy the same position in the LBD, making identical interactions with helix 12; however, the *N*-methyl group of R357A assumes a different conformation (C14—C15—N16—C17 torsion angle of −86° *versus* 70°, respectively), with its methyl group pointing towards the Leu353 side chain (Supplementary Fig. S3). OMIT maps calculated around the two molecules of the ligand are shown in Supplementary Figs. S4(*a*) and S4(*b*).

3.6. Spectroscopic characterization of PPARγ WT and F360L

The near-UV CD spectrum of wild-type PPARγ, a protein lacking tryptophan residues, shows a strong positive contribution centred at around 263 nm flanked by two positive shoulders at 270 and 258 nm and accompanied by fine structure features at 275–285 nm (Fig. 8*a*). The F360L mutant displays a near-UV CD spectrum similar to that of the WT but with a different intensity and with one of the positive shoulders blue-shifted to around 268 nm. The fluorescence emission spectra of WT and F360L are similar, but not identical, with a maximum emission wavelength centred around 308 nm characteristic of a tyrosine contribution (Fig. 8*b*).

The far-UV CD spectra of PPARγ WT and F360L are typical of a highly α-helical structure, showing local minima at around 208 and at 222 nm and a zero intercept at around 200 nm. Notably, the ratio of the molar ellipticity at 222 and 208 nm ($[\Theta]_{222}/[\Theta]_{208}$) is 0.938 and 0.859 for the WT and F360L, respectively (Fig. 8*c*), suggesting that the inter-helical interactions are decreased in F360L (Choy *et al.*, 2003).

3.7. Thermal unfolding

The thermal stability was investigated by continuously monitoring the ellipticity changes at 222 nm in the tempera-

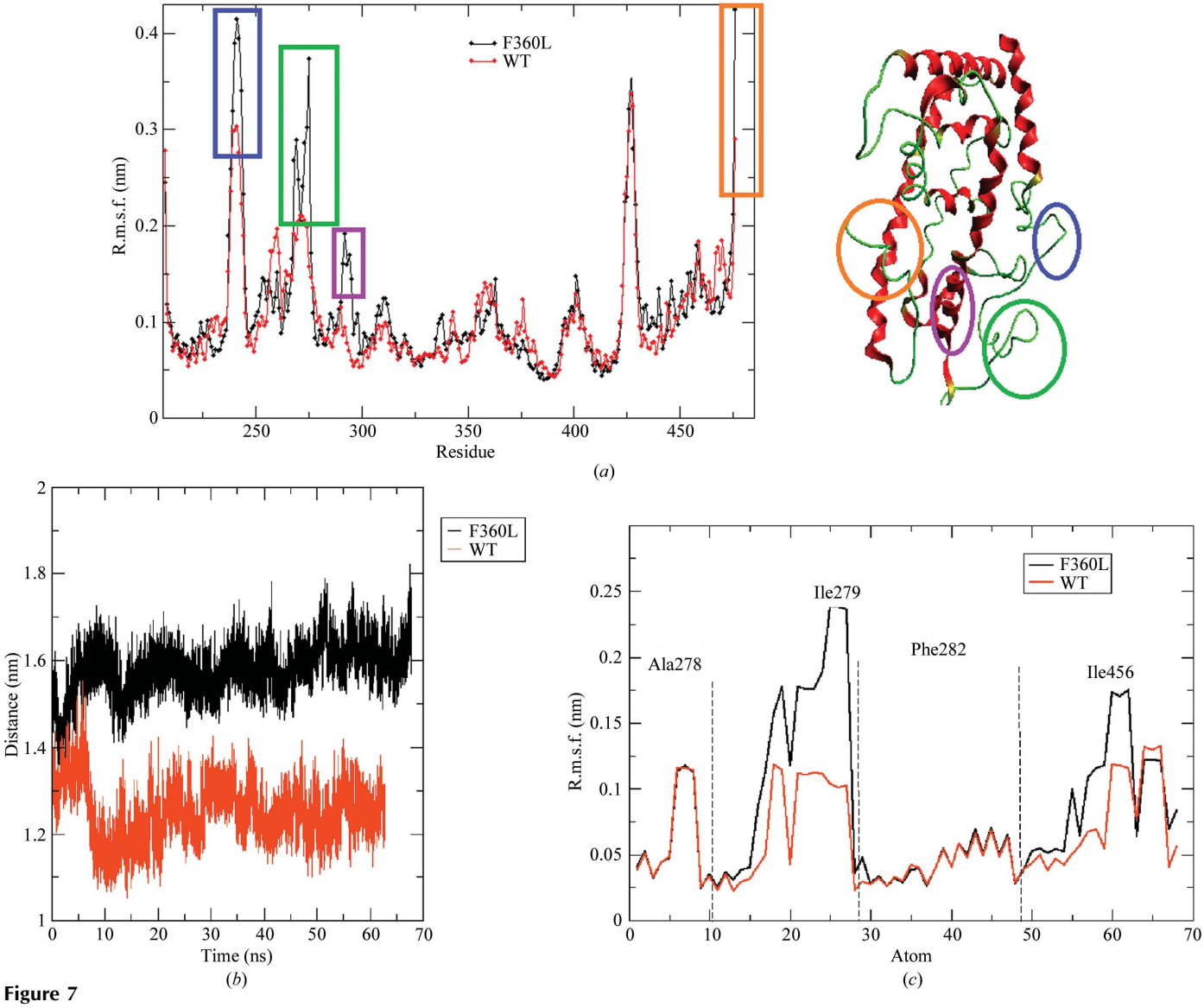

Figure 7
(*a*) C$^{\alpha}$ root-mean-square fluctuation (r.m.s.f.) for the WT and F360L. Marked regions refer to the specific protein portions highlighted in the inset, characterized by a sharp increase in r.m.s.f. from the WT to F360L. (*b*) Time course of the distance between the centre of the mass of helix 12 and the subportion 280–287 of the α-helix. (*c*) Root-mean-square fluctuation of residues Ala278, Ile279, Phe282 and Ile456.

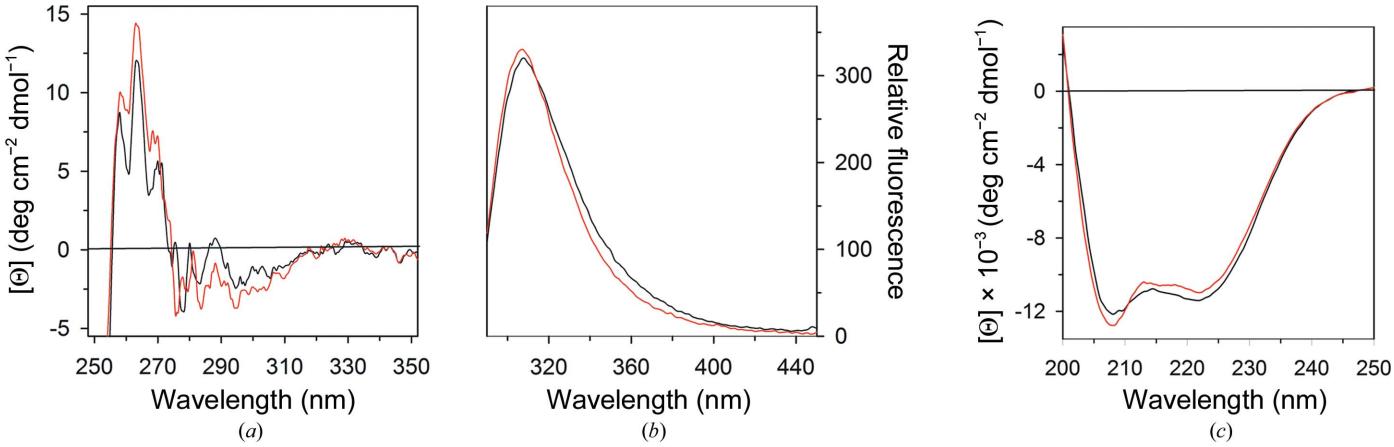

Figure 8
Spectroscopic properties of PPARγ WT (black) and F360L (red). (*a*) Near-UV CD spectra were recorded in a 1 cm path-length quartz cuvette at 4.60 mg ml^{-1} protein concentration (2.0 m*M* DTT) in 50 m*M* Tris–HCl pH 8.0 containing 0.20 *M* NaCl. (*b*) Intrinsic fluorescence emission spectra were recorded at 90.0 µg ml^{-1} protein concentration (274 nm excitation wavelength) in 20 m*M* Tris–HCl pH 8.0 containing 0.1 *M* NaCl and 0.2 m*M* DTT. (*c*) Far-UV CD spectra were recorded in a 0.01 cm path-length quartz cuvette at 4.60 mg ml^{-1} protein (2.0 m*M* DTT) in 50 m*M* Tris–HCl pH 8.0 containing 0.20 *M* NaCl.

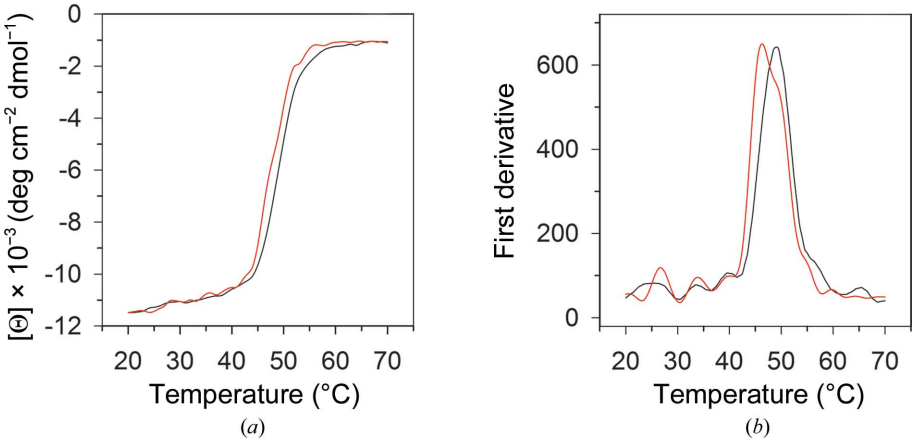

Figure 9
Thermal unfolding of PPARγ WT and F360L. (*a*) PPARγ WT (black) and F360L (red) were heated from 293 to 343 K in a 0.1 cm path-length quartz cuvette at 0.2 mg ml^{-1} in 20 m*M* Tris–HCl pH 8.0 containing 0.20 *M* NaCl and 0.2 m*M* DTT. The dichroic activity at 222 nm was monitored continuously every 0.5 K. (*b*) First derivative of the data shown in (*a*).

ture range 293–343 K (Fig. 9*a*). The parameter chosen to compare the transition curves of PPARγ WT and F360L is the melting temperature (T_m), defined as the midpoint of the denaturation process as calculated by plotting the first derivative of the molar ellipticity values as a function of temperature (Fig. 9*b*). The temperature-induced ellipticity changes at 222 nm, where the main amplitude was observed, occur in an apparent cooperative transition, with T_m values of 322 and 319.5 K for WT and F360L, respectively (Fig. 9*b*).

3.8. ITC experiments: the co-activator SRC-1 has a lower binding affinity for the mutants

ITC experiments were performed by injecting the co-activator SRC-1 into a cell containing PPARγ WT, PPARγ F360L or PPARγ R357A pre-equilibrated with LT175. The results showed that the WT recruits the coactivator with higher affinity with respect to the mutants (K_a = 7.64 ± 1.17 × 10^5 M^{-1} *versus* K_a = 3.01 ± 0.54 × 10^5 M^{-1} and K_a = 1.79 ± 0.28 × 10^5 M^{-1}, respectively; Supplementary Figs. S5*a*–S5*c*).

3.9. PPAR transcription activity

The transcription activity of WT PPARγ, PPARγ F360L and PPARγ R357A was evaluated in the presence of the full agonist rosiglitazone and LT175. For this purpose, Gal4–PPAR chimeric receptors were expressed in transiently transfected HepG2 cells according to a previously reported procedure (Pinelli *et al.*, 2005). As shown in Fig. 10(*a*), the efficacy of rosiglitazone remained basically unchanged towards WT and point-mutated PPARγ receptors. On the contrary, rosiglitazone displayed a remarkable lowering of potency; its EC_{50} value was 15-fold and sevenfold higher against PPARγ F360L and PPARγ R357A, respectively, compared with WT PPARγ (Table 3). A similar behaviour was observed for LT175; the efficacy towards the WT and both mutants remained basically unchanged, but the potency was reduced (Fig. 10*b*). However, the EC_{50} values turned out to be only 1.5-fold and twofold higher against PPARγ R357A and PPARγ F360L, respectively, compared with WT PPARγ (Table 3).

4. Discussion

In light of the crystal structures of PPARγ F360L complexed with LT175 and of PPARγ R357A with rosiglitazone, and of the MD simulations and CD experiments made on the apo form of the F360L mutant, it is possible to make the following considerations: (i) the Phe360 residue plays a key role in

stabilizing the facing H3 and H11 helices and loop 11/12 (Supplementary Figs. S6*a* and S6*b*) and a simple mutation to leucine leads to a lack of important van der Waals interactions with Ile residues belonging to H3 and H11 (Ile279 and Ile456); (ii) the F360L mutation is also responsible for the weakening of two important salt bridges connecting H3 and loop 11/12 through the residue Arg357 in loop 6/7; (iii) the R357A mutation confirms the importance of this residue in the global stabilization of the entire LBD; and (iv) the consequent destabilization and rearrangement of loop 11/12 in the mutant apo form elicits increased dynamics of H12, as shown by the MD simulation.

It must be noted that the inactive conformation of helix 12 observed in the crystal structure of the complex with the F360L mutant is clearly an artefact of the crystal packing, wherein the new stable dimer interface allows helix 12 of one monomer to protrude towards the ligand bound to the other monomer and to form a hydrogen bond to it, and *vice versa*. However, such a marked deviation of H12 from its active conformation would not be possible without the F360L mutation, which strongly destabilizes the region including H11, H3 and loop 11/12 (the diphenyl pocket), allowing the formation of a new dimer interface. In the absence of ligands with agonist activity an increase in the H12 dynamics and a stronger fluctuation of some regions of the LBD is probable, as indicated by the MD simulation and by the decrease of inter-helical interactions in F360L suggested by the far-UV CD experiments.

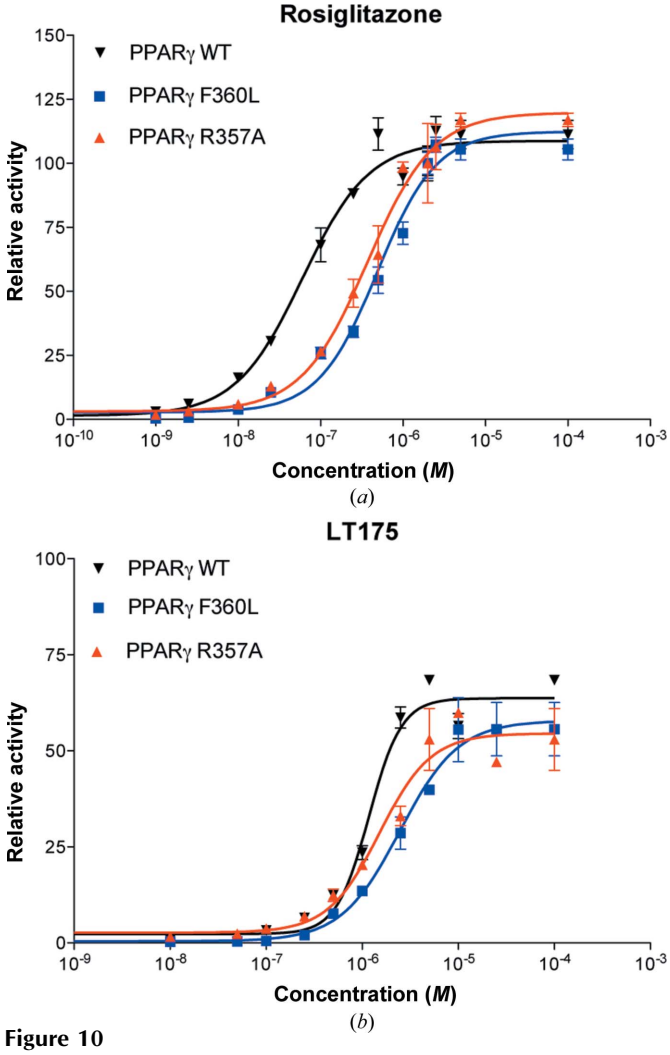

Figure 10
Transcription activity of rosiglitazone (*a*) and LT175 (*b*) towards PPARγ, PPARγ F360L and PPARγ R357A in a PPARγ Gal4-based assay. Results are expressed as a percentage of the efficacy and each point is the mean ± SEM of two experiments each performed in duplicate wells.

Table 3
Potency of rosiglitazone and LT175 towards PPARγ, PPARγ F360L and PPARγ R357A as determined in the PPARγ Gal4-based assay.

EC_{50} (n*M*)	WT PPARγ	F360L	R357A
Rosiglitazone	53 ± 17	790 ± 70	380 ± 70
LT175	1100 ± 180	2500 ± 500	1530 ± 270

A more disordered conformation of PPARγ helix 12 in the classic heterodimer interface with RXRα would impair efficient recruitment of the co-activator, because, as is known, this helix forms part of the hydrophobic cleft used to bind the co-activator (Nolte *et al.*, 1998). A less efficient recruitment of co-activator SRC-1 was also observed in the ITC experiments with F360L and R357A. In conclusion, it is reasonable to suppose that the destabilization of loop 11/12 and the terminal end of H11, as observed in the crystal structure of F360L–LT175 and also in the MD simulation and CD experiments on the apo form of the mutant, would impair the H12 dynamics and reduce the population of active conformations of the heterodimer able to recruit co-activators, therefore lowering the transactivation activity. In fact, the potency of LT175 towards the mutant is less than half of that towards the WT (Table 3). The transactivation curves for F360L (Fig. 10) show that both rosiglitazone and LT175 are able to restore the same efficacy to the WT, but their potency towards the mutant is reduced (for LT175 by a lesser extent, twofold *versus* 15-fold; see Table 3). Since LT175 occupies the diphenyl pocket, which is very close to the loop containing the mutation, it might be able to better counterbalance, with respect to rosiglitazone, the conformational instability induced by the mutation.

Finally, it must be noted that the Phe360 residue is highly conserved among all members of the PPAR gene family (Nolte *et al.*, 1998). The crucial role of this residue in LBD stability is confirmed by the fact that its mutation to the very similar leucine is able to induce dramatic conformational changes in the tertiary structure. The loss of important van der Waals interactions made by Phe360 and the subsequent loss of the salt bridge formed by Arg357 with a residue in loop 11/12 induces a conformational rearrangement of this loop and, in turn, increased mobility of helix 12. This larger disorder of H12 results in less efficient binding of the co-activator in the hydrophobic cleft.

In conclusion, the elucidation of the crystal structure of the PPARγ F360L–LT175 complex has provided considerable insights into the structural basis of the transactivation deficiency of this mutant, which has been associated with familial partial lipodystrophy.

We would like to thank the Biocrystal Facility at the CNR Institute of Biology and Molecular Pathology, La Sapienza University of Rome for the use of the Phoenix robot for crystallization trials. We would also like to thank Professor Miriam Rossi of Vassar College, New York for carefully reading the manuscript.

References

Adams, P. D. *et al.* (2010). *Acta Cryst.* D**66**, 213–221.
Agostini, M. *et al.* (2006). *Cell Metab.* **4**, 303–311.
Al-Shali, K., Cao, H., Knoers, N., Hermus, A. R., Tack, C. J. & Hegele, R. A. (2004). *J. Clin. Endocrinol. Metab.* **89**, 5655–5660.
Amadei, A., Linssen, A. B. & Berendsen, H. J. C. (1993). *Proteins*, **17**, 412–425.
Anghel, S. I. & Wahli, W. (2007). *Cell Res.* **17**, 486–511.
Balamurugam, B. *et al.* (2007). *J. Appl. Cryst.* **40**, 773–777.
Barroso, I., Gurnell, M., Crowley, V. E., Agostini, M., Schwabe, J. W., Soos, M. A., Maslen, G. L., Williams, T. D., Lewis, H., Schafer, A. J., Chatterjee, V. K. & O'Rahilly, S. (1999). *Nature (London)*, **402**, 880–883.
Battye, T. G. G., Kontogiannis, L., Johnson, O., Powell, H. R. & Leslie, A. G. W. (2011). *Acta Cryst.* D**67**, 271–281.
Berendsen, H. J. C., Postma, J. P. M., van Gunsteren, W. F. & Hermans, J. (1981). *Intermolecular Forces*, edited by B. Pullman, pp. 331–342. Dordrecht: Reidel.
Berendsen, H. J. C., Postma, J. P. M., van Gunsteren, W. F., DiNola, A. & Haak, J. R. (1984). *J. Chem. Phys.* **81**, 3684.
Brünger, A. T., Adams, P. D., Clore, G. M., DeLano, W. L., Gros, P., Grosse-Kunstleve, R. W., Jiang, J.-S., Kuszewski, J., Nilges, M., Pannu, N. S., Read, R. J., Rice, L. M., Simonson, T. & Warren, G. L. (1998). *Acta Cryst.* D**54**, 905–921.
Chan, K. H. K., Niu, T., Ma, Y., You, N. C., Song, Y., Sobel, E. M., Hsu, Y.-H., Balasubramanian, R., Qiao, Y., Tinker, L. & Liu, S. (2013). *J. Clin. Endocrinol. Metab.* **98**, E600–E604.
Chandra, V., Huang, P., Hamuro, Y., Raghuram, S., Wang, Y., Burris, T. P. & Rastinejad, F. (2008). *Nature (London)*, **456**, 350–356.
Chen, V. B., Arendall, W. B., Headd, J. J., Keedy, D. A., Immormino, R. M., Kapral, G. J., Murray, L. W., Richardson, J. S. & Richardson, D. C. (2010). *Acta Cryst.* D**66**, 12–21.
Choy, N., Raussens, V. & Narayanaswami, V. (2003). *J. Mol. Biol.* **334**, 527–539.
Darden, T., York, D. & Pedersen, L. (1993). *Chem. Phys.* **98**, 10089.
Evans, R. M., Barish, G. D. & Wang, Y.-X. (2004). *Nature Med.* **10**, 355–361.
Flocco, M. M. & Mowbray, S. L. (1994). *J. Mol. Biol.* **235**, 709–717.
Guettier, J.-M., Park, J. Y., Cochran, E. K., Poitou, C., Basdevant, A., Meier, M., Clément, K., Magré, J. & Gorden, P. (2008). *Clin. Endocrinol.* **68**, 547–554.
Hegele, R. A. (2005). *Int. J. Obes. (Lond.)*, **29**, Suppl. 1, S31–S35.
Hegele, R. A., Cao, H., Frankowski, C., Mathews, S. T. & Leff, T. (2002). *Diabetes*, **51**, 3586–3590.
Hess, B., Bekker, H., Berendsen, H. J. C. & Fraaije, J. G. E. M. (1997). *J. Comput. Chem.* **18**, 1463–1470
Hollon, T. & Yoshimura, F. K. (1989). *Anal. Biochem.* **182**, 411–418.
Jeninga, E. H., Gurnell, M. & Kalkhoven, E. (2009). *Trends Endocrinol. Metab.* **20**, 380–387.
Jorgensen, W. L., Maxwell, D. S. & Tirado-Rives, J. (1996). *J. Am. Chem. Soc.* **118**, 11225–11236.
Kabsch, W. (2010). *Acta Cryst.* D**66**, 125–132.
Kersten, S., Desvergne, B. & Wahli, W. (2000). *Nature (London)*, **405**, 421–424.
Lehrke, M. & Lazar, M. A. (2005). *Cell*, **123**, 993–999.
Li, G. & Leff, T. (2007). *Mol. Endocrinol.* **21**, 857–864.
Mandard, S. & Patsouris, D. (2013). *PPAR Res.* **2013**, 613864.
Meirhaeghe, A. & Amouyel, P. (2004). *Mol. Genet. Metab.* **83**, 93–102.
Michalik, L. & Wahli, W. (2006). *J. Clin. Invest.* **116**, 598–606.
Monajemi, H., Zhang, L., Li, G., Jeninga, E. H., Cao, H., Maas, M., Brouwer, C. B., Kalkhoven, E., Stroes, E., Hegele, R. A. & Leff, T. (2007). *J. Clin. Endocrinol. Metab.* **92**, 1606–1612.
Montanari, R., Saccoccia, F., Scotti, E., Crestani, M., Godio, C., Gilardi, F., Loiodice, F., Fracchiolla, G., Laghezza, A., Tortorella, P., Lavecchia, A., Novellino, E., Mazza, F., Aschi, M. & Pochetti, G. (2008). *J. Med. Chem.* **51**, 7768–7776.
Murshudov, G. N., Skubák, P., Lebedev, A. A., Pannu, N. S., Steiner, R. A., Nicholls, R. A., Winn, M. D., Long, F. & Vagin, A. A. (2011). *Acta Cryst.* D**67**, 355–367.
Navaza, J. (1994). *Acta Cryst.* A**50**, 157–163.
Nolte, R. T., Wisely, G. B., Westin, S., Cobb, J. E., Lambert, M. H., Kurokawa, R., Rosenfeld, M. G., Willson, T. M., Glass, C. K. & Milburn, M. V. (1998). *Nature (London)*, **395**, 137–143.
Pinelli, A., Godio, C., Laghezza, A., Mitro, N., Fracchiolla, G., Tortorella, V., Lavecchia, A., Novellino, E., Fruchart, J. C., Staels, B., Crestani, M. & Loiodice, F. (2005). *J. Med. Chem.* **48**, 5509–5519.
Pochetti, G., Godio, C., Mitro, N., Caruso, D., Galmozzi, A., Scurati, S., Loiodice, F., Fracchiolla, G., Tortorella, P., Laghezza, A., Lavecchia, A., Novellino, E., Mazza, F. & Crestani, M. (2007). *J. Biol. Chem.* **282**, 17314–17324.
Raspé, E., Madsen, L., Lefebvre, A. M., Leitersdorf, I., Gelman, L., Peinado-Onsurbe, J., Dallongeville, J., Fruchart, J. C., Berge, R. & Staels, B. (1999). *J. Lipid Res.* **40**, 2099–2110.
Sarraf, P., Mueller, E., Smith, W. M., Wright, H. M., Kum, J. B., Aaltonen, L. A., de la Chapelle, A., Spiegelman, B. M. & Eng, C. (1999). *Mol. Cell*, **3**, 799–804.
Savage, D. B. *et al.* (2003). *Diabetes*, **52**, 910–917.
Schoonjans, K. & Auwerx, J. (2000). *Lancet*, **355**, 1008–1010.
Semple, R. K., Chatterjee, V. K. & O'Rahilly, S. (2006). *J. Clin. Invest.* **116**, 581–589.
Tan, G. D., Savage, D. B., Fielding, B. A., Collins, J., Hodson, L., Humphreys, S. M., O'Rahilly, S., Chatterjee, K., Frayn, K. N. & Karpe, F. (2008). *J. Clin. Endocrinol. Metab.* **93**, 4462–4470.
Tontonoz, P. & Spiegelman, B. M. (2008). *Annu. Rev. Biochem.* **77**, 289–312.
Van Der Spoel, D., Lindahl, E., Hess, B., Groenhof, G., Mark, A. E. & Berendsen, H. J. C. (2005). *J. Comput. Chem.* **26**, 1701–1718.
Wang, T., Xu, J., Yu, X., Yang, R. & Han, Z. C. (2006). *Crit. Rev. Oncol. Hematol.* **58**, 1–14.
Zoete, V., Grosdidier, A. & Michielin, O. (2007). *Biochim. Biophys. Acta*, **1771**, 915–925.